Almeida, Humberto; Lisbôa, Tales; Spickenheuer, Axel; St-Pierre, Luc

A sequential finite element model updating routine to identify creep parameters for filament wound composite cylinders in aggressive environments

Published in:
Computers & Structures

DOI:
10.1016/j.compstruc.2022.106939

Published: 01/02/2023

Document Version
Publisher's PDF, also known as Version of record

Please cite the original version:
Almeida, H., Lisbôa, T., Spickenheuer, A., & St-Pierre, L. (2023). A sequential finite element model updating routine to identify creep parameters for filament wound composite cylinders in aggressive environments. *Computers & Structures*, *276*, Article 106939. https://doi.org/10.1016/j.compstruc.2022.106939

Computers and Structures 276 (2023) 106939

Contents lists available at ScienceDirect

Computers and Structures

journal homepage: www.elsevier.com/locate/compstruc

A sequential finite element model updating routine to identify creep parameters for filament wound composite cylinders in aggressive environments

José Humberto S. Almeida Jr [a,b,*], Tales V. Lisbôa [c], Axel Spickenheuer [c], Luc St-Pierre [b]

[a] Advanced Composites Research Group, School of Mechanical and Aerospace Engineering, Queen's University Belfast, Belfast, UK
[b] Department of Mechanical Engineering, Aalto University, Espoo, Finland
[c] Leibniz-Institut für Polymerforschung Dresden e.V., Hohe Str. 6, Dresden, Germany

ARTICLE INFO

Article history:
Received 28 June 2022
Accepted 17 November 2022

Keywords:
Creep modelling
Finite element model updating
Genetic algorithm
Gradient–based algorithm
Filament winding

ABSTRACT

In this paper, a Finite Element Model Updating (FEMU) procedure is developed to find the best creep parameters for filament-wound cylinders under radial compression in harsh environmental conditions. Three winding angles are considered, each under three different hygrothermal conditions. The two–stage creep model captures i) primary creep through a time–hardening approach whilst ii) secondary creep is captured by Norton's law. Given the high number of parameters in this two–stage creep model and the complexity of determining them experimentally, the FEMU routine utilises an optimisation scheme that sequentially couples a Genetic Algorithm (GA) with a gradient-based (GB) Levenberq-Marquardt Algorithm (LMA) to find all required creep input parameters to feed the model that best simulates experimental results. This framework finds the global optimum through an initial screening of the optimum area within the design space with GA, clearing the path to allow the GB algorithm to find the global optimum, substantially reducing the chance or even avoiding falling in local minima. The global search is driven by experimental data of cylinders loaded in radial compression under aggressive environments. The numerical results show excellent agreement with experimental results with reasonably low computational efforts.

1. Introduction

Filament winding (FW) is the most suited manufacturing process for axisymmetric structures, e.g., tubes [1], cylinders [2], and pressure vessels [3]. The automation of FW enables simultaneous production of identical parts, which also facilitates large volume productions, entailing a decrease in the overall manufacturing costs [4]. The FW process is also suitable to produce large carbon fibre–reinforced polymer (CFRP) composite components, for example, the Vega satellite launcher (European Space Agency) and Boeing 787 fuselage. Another remarkable characteristic is the utilisation of long continuous fibres, which allows the designing of structures with high stiffness and strength at the minimum possible weight [5].

The CFRP components usually operate at high temperatures and in humid environments, which affect their mechanical response over time [6–8]. The behaviour of the structure is then dependent on the combination of temperature and time, which affect their creep rate [9]. This set of parameters has a more pronounced effect when the structure is laminated with off–axis layers, which can generate premature micro-cracks, resin plasticization, and fibre–matrix interface weakening [10]. These micro-damages are generated due to the viscoelastic nature of polymer matrices, which exhibit a time-dependent behaviour and, hence, are sensitive to both hygrothermal and temperature effects [11–13]. Therefore, the design of such CFRP structures must consider creep and ageing degradation that might affect the lifespan of the composite component [14–16].

Experiments to characterise the long-term properties of composites are avoided or reduced, when possible, given the high cost and time involved in such tests [16]. Therefore, computational models able to determine such long-term behaviour of composites have been developed to fully or partially replace experiments. Focussing specifically on composite cylinders, they usually operate under transverse loads, either in underground or above-ground applications, causing changes in their cross-section shape, where perfect cylinders become elliptical ones [17]. This radial deforma-

* Corresponding author.
E-mail address: humberto.almeida@qub.ac.uk (J.H.S. Almeida Jr).

https://doi.org/10.1016/j.compstruc.2022.106939
0045-7949/

tion increases with time due to the viscoelastic nature of the polymer, which makes predicting such long-term properties a challenge [18,19].

Several higher–order theories have been developed over the last decades to predict the short– and long–term properties of beams, plates, and shells [20]. The most well disseminated higher–order theories include Carrera's (CUF) [21–23] and Generalised Unified Formulations (GUF) [24]. An accurate calculation of internal stresses in laminated composites, in particular thick laminates, is essential to properly design lightweight components. According to Carrera [25], there are three main approaches: continuum base, asymptotic or axiomatic theories. Each of these theories has a different formulation to predict displacement, strain and stress fields [26]. In this case, Unified Formulations are very attractive since the unified solution method can be chosen according to the problem by easily changing the expansion functions/terms [27], which might reflect in more precise failure predictions for composite structures.

Indeed, CFRP structures are designed to not fail by creep, however, their mechanical performances can be hugely affected by creep deformation. Hence, the development of computational models to predict creep stages over time are of utmost importance. The creep deformation process can be divided into three stages: primary, secondary, and tertiary [28]. In the primary or transient stage, the strain rate is high but decreases with time and strain since the structure has an increase in both creep strength and strain hardening. Secondary creep is a steady–state stage, where the deformation rate decreases substantially and strain increases slowly over time. In tertiary creep, a sudden increase in the creep rate takes place, leading to the eventual failure of the system [29].

Computational models to predict creep deformation have been developed [9,30,31], however a common issue in high–fidelity models is the large number of input parameters needed. Determining all these input parameters experimentally is often deemed too expensive and/or time-consuming. To this end, Lisbôa et al. [32] developed a finite element model updating (FEMU) routine to approximate simulations to experimental observations [33–35]. FEMU is a sensitivity approach to update input properties that best correlate to target results, for instance, experimental results [36]. The expected outcome of a well–developed FEMU algorithm is a more efficient finite element (FE) framework, wherein the influence of uncertainties is minimised through the iterative updating procedure of input values.

To the best of our knowledge, there is no work in the literature reporting the optimal set of input parameters to simulate creep in composites. Existing methods often rely on simple curve-fitting techniques using empirical power–law models, such as Burger's [37] and Findley's [13] approaches. In these models, the number of input parameters is small and it is straightforward to find the best input parameters with simple algorithms. Both models are empirical and, hence, not constitutive laws. Consequently, the evaluation and calculation of stresses over time are neither accurate nor feasible. This paper aims to overcome this limitation, by developing a consistent 2–stage creep model assisted by a robust and computationally–efficient framework to find the best set of input parameters to simulate experimental observations. The framework is developed for composite cylinders under radial compression and in aggressive environments.

In this paper, we develop an original multi–level FEMU framework to obtain the best set of input parameters to predict primary and secondary creep stages for CFRP filament wound composite cylinders under radial compression loading. Another key novelty is the determination of the best input values for the cylinders under different hygrothermal conditions. The two creep stages are modelled here, where a time–hardening approach is used to predict primary creep, whilst secondary creep is modelled through a Norton–based model. Given that the cost function for both creep problems may have several local minima, a multi–level framework is developed combining i) gradient–free optimisation routine (genetic algorithm – GA) to evaluate the objective function of the optimisation problem globally, that is, it is used to find the region in which the global minimum is; ii) followed by a gradient–based (GB) algorithm using the optimum results from GA as its starting point to find the global minimum, strongly reducing the chance of falling into local minima.

2. Experimental details

A dedicated creep testing equipment was designed and fabricated to evaluate the behaviour of composite cylinders under radial compressive loading in high temperature and humid environments [13]. The experimental setup is shown in Fig. 1.

The cylinders were designed using the CadWind software and manufactured by FW using a KUKA 140 L100 robot with towpregs from Toray (T700-12 K-50C fibre and UF3369 epoxy resin). The cylinders produced had a fibre volume fraction (V_f) of 70% [12]. The cylinders were manufactured onto a stainless-steel mandrel with a diameter of 50.8 mm and a length of 1 mm. Curing was performed in an oven with air circulation for 5 h at 120 °C. The cylinders were then cooled down and extracted from the mandrel. Afterwards, the specimens were cut off at the desired length of 50 mm.

The cylinders were manufactured with three different winding angles: $[\pm 60], [\pm 75]$, and $[\pm 90]$ (actually wound at $[\pm 89.6]$). The first two configurations ($[\pm 60]$ and $[\pm 75]$) have a helical winding trajectory while the last one ($[\pm 90]$) has a hoop winding trajectory. The helical specimens were produced with a winding pattern of 1:1 [2]. Moreover, three different environmental conditions were considered: room temperature, that is, with mechanical loading only (**ML**), water at room temperature (**WRT**) and hot water (40 °C) (**HW**). Room temperature is considered 23 °C and relative humidity is 50%.

All cylinders were then subjected to long–term radial compression [39] at 25% of their ultimate load (static tests were carried out in [38]). The specimens were kept under compression and in these environmental conditions for 10 days (240 h). Prior to the creep tests, both **WRT** and **HW** samples were placed in water to determine their water uptake (WU) until equilibrium was reached. The thickness, applied force and water uptake for all tests are summarised in Table 1.

3. The FEMU framework

The FEMU is a procedure to fine-tune or identify unknown parameters by adjusting a parametrized FE model and comparing the results against experimental data [32]. An optimisation procedure is used to propose new sets of input parameters that will move the simulation closer to the experiment. A usual drawback of such a procedure is a local minimum, which refers to a minimum within a neighbourhood that may not be the global minimum. In order to decrease or even avoid the probability of falling into a local minimum, a sequential procedure using the genetic algorithm (GA) and Levenberg-Marquart Algorithm (LMA) is herein developed. A flowchart describing the sequential procedure is depicted in Fig. 2. Details of each step are provided next.

Fig. 3 shows the FEMU procedure at a glance. In a *direct* approach, the geometry, boundary conditions (BC), and material behaviour are known. An FE model is built to obtain the mechanical response of the structure. With FEMU, the problem is solved in an *indirect* fashion. First, a numerical model is developed, in which the unknowns are based on initial guesses, and its predictions are

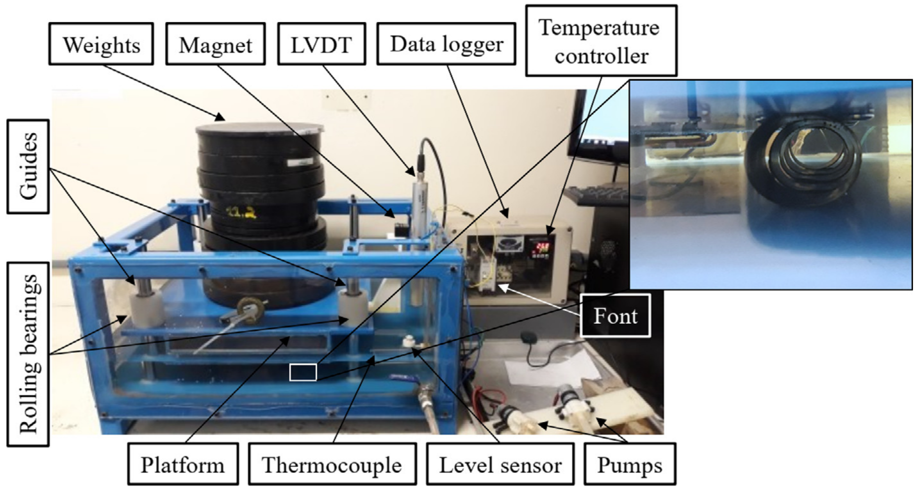

Fig. 1. Details of the used equipment for creep tests (adapted from [13]).

Table 1
Stacking sequence, thickness, applied forces, and water uptake for all cylinders.

Winding Angle	Conditioning	Thickness [mm]	Force [N]	WU (M_∞) [%]
[±60]	**ML**	0.72 ± 0.02	135.0	-
	WRT			0.506 ± 0.035
	HW			1.784 ± 0.016
[±75]	**ML**	0.77 ± 0.05	181.5	-
	WRT			0.399 ± 0.085
	HW			1.601 ± 0.107
[±90]	**ML**	0.70 ± 0.01	203.0	-
	WRT			0.357 ± 0.036
	HW			1.716 ± 0.107

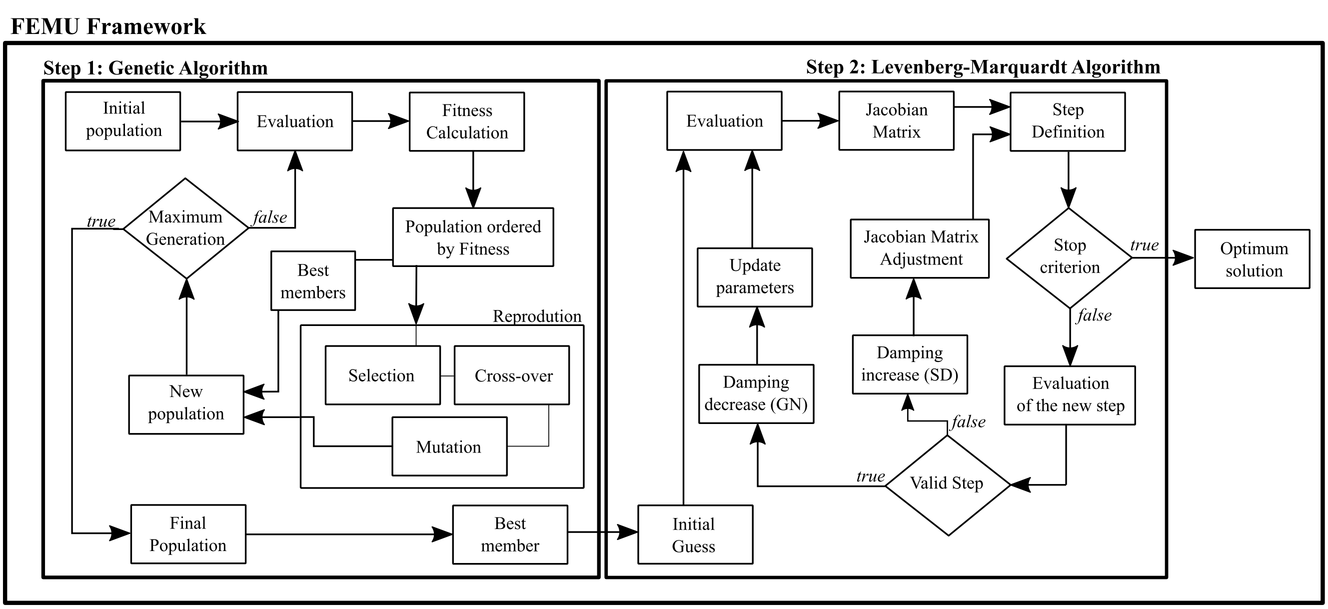

Fig. 2. Flowchart of the sequential optimisation procedure.

compared to experimental tests. Second, the input parameters are adjusted to minimise the difference between simulations and experiments. This adjustment is usually done with an optimisation scheme coupled with the parameterised FE model. Thus, FEMU solves the direct problem to compare the simulation output with experimental data, whereas the inverse problem represents a conceptualisation of the framework procedure.

3.1. The FE Model

The FE model is depicted in Fig. 4, wherein all details of the FE problem are shown. In order to add realism in terms of modelling as–manufactured structures, the geometry is constructed considering the filament winding pattern following the methodology proposed by Lisbôa et al. [32]. Triangular finite elements were used

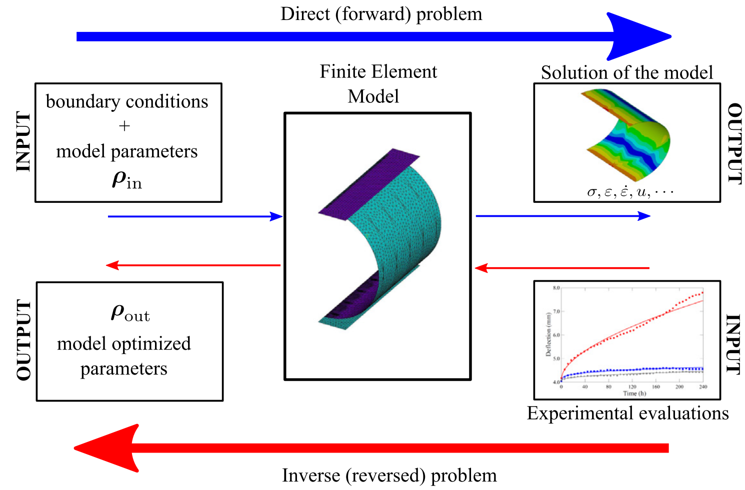

Fig. 3. Schematic illustration of a direct × inverse problem highlighting the FEMU framework developed.

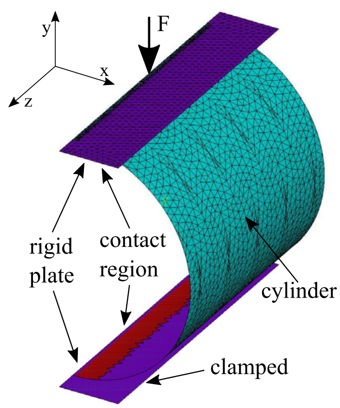

Fig. 4. The developed FE model and its relevant details.

given the winding pattern formed during the manufacturing of filament wound structures, which have diamond–like shapes. Due to this winding pattern characteristic, it is unfeasible to use rectangular elements, for instance. According to Lisbôa et al. [2,32], considering this manufacturing signature in the FE modelling aids in realism towards modelling filament wound structures and, hence, provides more accurate predictions when compared to conventional approaches, in which a nominal winding angle is assigned to each ply.

Since the problem is symmetric, a symmetry plane is used to partition the cylinder in half. Initial simulations on full–models have been carried out and the results were identical to those of the half–size models. Therefore, a half–size model is thereafter considered for computational efficiency. A vertical compressive force is applied to the top platen, and therefore the radial displacement is released, whereas all other degrees of freedom are restricted. The bottom rigid platen is fully clamped. No BCs are applied to the cylinder, with the exception of the contact between the platens and the cylinder (Fig. 4). The FE modelling is performed using Ansys APDL 2021 R1 FE platform, which is well–suited to generate parametric FE models. A 4-node shell element in its degenerated triangular shape with an equivalent single–layer formulation is utilised in the converged mesh (shown in Fig. 4). The problem is non-linear due to the contact and large displacements, thus geometric nonlinearity is considered in all simulations and the Newton–Raphson method is used to solve the FE problem. A surface–to–surface contact algorithm (with an augmented Lagrangian) is utilised to model the interaction between the sample and compressive platens.

3.2. Norm definition

Since two different optimisation approaches are used in a sequential manner, the norm (distance between numerical and experimental responses) must be defined in a way that can be used throughout the sequential framework. Furthermore, the GA considers fitness as the evaluation parameter whereas LMA uses the norm for the minimisation problem. The norm is then defined as:

$$\frac{1}{f_{it}} = L_2 = \frac{1}{n_{pts}} \sqrt{\boldsymbol{y}^{\mathrm{T}} \boldsymbol{W} \boldsymbol{y}}, \tag{1}$$

where f_{it} is the fitness, $\boldsymbol{y}$ are the residuals and $\boldsymbol{W}$ is the weighting matrix. The fitness is a GA parameter and it defines how fit is the individual with respect to the environment and to other individuals while the residuals is a vector that contains the differences between experimental and numerical data in each evaluated point. The size of this vector is the number of points measuring the norm, n_{pts}. The residuals and the weighting matrix are written as:

$$y_i = d_i^{\mathrm{E}} - d_i^{\mathrm{N}}, \tag{2}$$

$$W_{ii} = \frac{1}{\left(d_i^{\mathrm{E}}\right)^2}, \tag{3}$$

where d_i^{N} and d_i^{E} are numerical and experimental responses at the i-th position, respectively. This means that the outputs of the FE model are load and displacement, where FEMU evaluates every point of the experimental curve. This is a key strategy to minimise the error and approximate simulations to experiments.

According to Eqs. (1), (2) and (3), the norm is a percentile one. It is straightforward to see that the closer the simulation is to the experiment, the smaller the y_i and L_2 are. Likewise, a closer response will develop a larger fitness, which plays an important role in the GA as such individuals are to be preferred in the selection for reproduction.

3.3. FEMU – step 1: Genetic algorithm

The global flowchart of the sequential FEMU procedure is depicted in Fig. 2. A summary of the GA is as follows:

- Initially, an *initial population* is considered, wherein each individual is defined by a set of real-value parameters (*chromosomes*), $\boldsymbol{\rho}$, generated by a random uniform distribution of the parameters domain.
- This *population* is evaluated, i.e., the randomised parameters are inserted into the parametric FE model for obtaining the mechanical response of the cylinder.
- Numerical and experimental are compared through the L_2-norm (Eq. (1)), and the *fitness* of each individual is then calculated.
- *Individuals* (parents) are selected and, through *crossovers*, the new *individuals* (children) are created. A *mutation* chance is applied to each new *individual* and a new *population* is generated. The best members of the former population are also included in the new one.
- Then, the new members are evaluated and their *fitness* is calculated.
- This procedure is repeated for a particular number of *generations*, at which the optimisation procedure stops, and then a *final population* is reached.

After all populations are evaluated, the average fitness ($\bar{f}_{it}$) of each member is calculated, as follows:

$$\bar{f}_{it}^{(i)} = \frac{f_{it}^{(i)}}{\sum_{j}^{n_{ind}} f_{it}^{(j)}} \quad \therefore \quad \bar{f}_{it}^{(i)} \in (0,1), \tag{4}$$

where n_{ind} defines the population size (number of individuals). With the average fitness of each member defined, the reproduction procedures (selection, crossover, and mutation) are applied to the population. The parameters $r_i \in [0,1), i \in \mathbb{N}$, derived from a random uniform distribution, are used in this procedure to add the required randomness to the optimisation procedure.

Each reproduction selects individuals from the population. The crossover uses simulated binary crossover (SBX) [40]. Essentially, the children are defined by their parents as:

$$\rho_i^{(\alpha,n+1)} = \frac{1}{2}\left[r_v \rho_i^{(\alpha,n)} + (2 - r_v)\rho_i^{(\beta,n)}\right] \tag{5}$$

$$\rho_i^{(\beta,n+1)} = \frac{1}{2}\left[(2 - r_v)\rho_i^{(\alpha,n)} + r_v \rho_i^{(\beta,n)}\right], \tag{6}$$

where i corresponds to a particular chromosome in $\boldsymbol{\rho}$, α and β identify the parents, n defines the generation and:

$$r_v = \begin{cases} 1 + (2r)^{\frac{1}{\eta+1}}, & 0 \leqslant r < 0.5 \\ 1 + \left[\frac{1}{2(1-r)}\right]^{\frac{1}{\eta+1}}, & 0.5 \leqslant r < 1, \end{cases} \tag{7}$$

in which $\eta \in [0, \infty)$ is an "intensity" parameter. For small values $\eta < 2$, the children ($\boldsymbol{\rho}^{(\alpha,n+1)}$ and $\boldsymbol{\rho}^{(\beta,n+1)}$) are likely to be far away from the parents [40].

After a new population is generated, the individuals may mutate. A non-uniform mutation operator [41] is herein used. Initially, it is verified if the individual will mutate by generating an r number and comparing it with some predefined value, normally very small, that represents the likelihood of an individual being mutated. If the individual is mutated, then two other random numbers, r_1 and r_2, are independently generated for each gene. With r_1, one constructs δ, a "jump" function [41], as follows:

$$\delta_i = \begin{cases} U_i - \rho_i, & 0 \leqslant r_1 < 0.5 \\ L_i - \rho_i, & 0.5 \leqslant r_1 < 1, \end{cases} \tag{8}$$

where U_i and L_i define the upper and bottom limits of the i-th chromosome of $\boldsymbol{\rho}$ and, with r_2, defines its mutation as:

$$\rho_i^{(a,n+1)} := \rho_i^{(a,n+1)} + \delta\left[1 - r_2^{(1-n/n_{gen})^{\gamma}}\right], \tag{9}$$

in which n_{gen} corresponds to the maximum generation number and γ represents the degree of non-uniformity. Smaller values of γ tend to push the value of the chromosome away from its original value and the number of generations reduces the effect of the mutation in generations close to the final one.

After all these steps, a new population is constructed, considering the best members of the previous one, and evaluated again until the maximum number of generations is achieved. Then, the final solution is obtained.

3.4. FEMU – step 2: Levenberg–Marquardt Algorithm

The LMA is a gradient-based (GB) optimisation algorithm that is a mix between Gauss–Newton (GN) and the Steepest-Descent (SD) procedures [42]. Through a "damping factor", μ, the LMA moves from GN to SD methods and vice versa. When a large μ is used, the method switches to SD, whereas for small μ, it remains in the GN method [42].

The main fundamental relation of LMA reads:

$$\left(\mathbf{J}^{\mathrm{T}}\mathbf{J} - \mu\mathbf{I}\right)\Delta\boldsymbol{\rho} = -\mathbf{J}^{\mathrm{T}}\mathbf{y}, \tag{10}$$

where $\mathbf{J}$ corresponds to the Jacobian matrix, $\Delta\boldsymbol{\rho}$ defines the step size, and $\mathbf{I}$ is the identity matrix. The new step is defined as:

$$\boldsymbol{\rho} := \boldsymbol{\rho} + \Delta\boldsymbol{\rho}, \tag{11}$$

The Jacobian matrix $\mathbf{J}$ is the variation of the residuals regarding the step and, numerically, are obtained by forwarding finite differences, as follows:

$$J_{ij} = \frac{\partial y_i}{\partial \rho_j} \approx \frac{y_i(\boldsymbol{\rho} + \delta_j \Delta\boldsymbol{\rho}) - y_i(\boldsymbol{\rho})}{\Delta \rho_j}, \tag{12}$$

noticing that $\delta_j \Delta\boldsymbol{\rho}$ refers to an evaluation only in the j–direction.

Revisiting Fig. 2, one observes that in LMA:

- The initial guess is the best member of the final population obtained through GA optimisation.
- Through an arbitrary increment of the initial step, the Jacobian matrix is constructed by evaluating some auxiliary analyses.
- By solving Eq. (10), $\Delta\boldsymbol{\rho}$ is obtained, and a new step, $\boldsymbol{\rho} + \Delta\boldsymbol{\rho}$, is evaluated.
- If the norm difference between the new and old analyses is above a tolerance, μ decreases, and the new set of design variables are updated and evaluated. otherwise, (in a non-valid step), μ increases, the Jacobian matrix is updated, and Eq. (10) is solved again for deriving a new step size.
- This cycle is completed when a tolerance in the step size is reached and the optimised solution is obtained.

The validity of the step is determined by the following relation:

$$\lambda = \frac{L_2(\boldsymbol{\rho}) - L_2(\boldsymbol{\rho} + \Delta\boldsymbol{\rho})}{\Delta\boldsymbol{\rho}^{\mathrm{T}}\left(\mu\Delta\boldsymbol{\rho} + \mathbf{J}^{\mathrm{T}}\mathbf{y}\right)}, \tag{13}$$

in which $\lambda > \epsilon$ and $\lambda < \epsilon$ correspond to a valid and invalid step, respectively, and $\epsilon \leqslant 0$.

The size of μ is related to the problem in the evaluation and its value is modified during the optimisation procedure in order to switch between the methods in an appropriate way. It is suggested to vary μ depending on the step's validity. Thus, μ is modified through an auxiliary positive parameter τ as follows:

$$\mu := \tau\mu, \tag{14}$$

where $\tau > 1$ when $\lambda < \varepsilon$ and $\tau < 1$ when $\lambda > \varepsilon$. In other words, in a valid step, LMA "switches" to GN, whereas for an invalid one, the method remains at SD.

For invalid steps, the Jacobian matrix is updated as:

$$J := J + \frac{1}{\Delta\boldsymbol{\rho}^{\mathrm{T}}\Delta\boldsymbol{\rho}}(\mathbf{y}^{\mathrm{i}+1} - \mathbf{y}^{\mathrm{i}} - \mathbf{J}\Delta\boldsymbol{\rho})\Delta\boldsymbol{\rho}^{\mathrm{T}}, \tag{15}$$

to improve the convergence where $\Delta\boldsymbol{\rho}$ is the step size that achieved the invalid step, as well as $\mathbf{y}^{\mathrm{i}+1}$ and $\mathbf{y}^{\mathrm{i}}$ correspond to the previous and actual residuals, respectively. For each valid step, the Jacobian matrix is recalculated through Eq. (12).

The L^{∞}-norm of the step size is considered as stopping criterion: the algorithm stops if this norm is below some preset tolerance. Thus, a mapping of the design variables is performed due to their different orders of magnitude.

For linear parameters, the transformation is a linear one, as follows:

$$g = \frac{(G-L)}{U-L} \quad \therefore \quad \Delta g = \frac{\Delta G}{U-L}, \tag{16}$$

while for logarithm ones, the mapping is defined as:

$$g = \frac{\ln G - \ln L}{\ln U - \ln L} \quad \therefore \quad \Delta g = \frac{\ln(\Delta G + G) - \ln G}{\ln U - \ln L}, \tag{17}$$

noticing that g and G correspond to parameters in the mapped and non-mapped domains, respectively. Essentially, the domains of non-mapped and mapped variables are $G \in [L, U]$ and $g \in [0, 1]$, respectively. This mapping is not required by the GA algorithm since the scale of the variables is insensitive to its performance.

3.5. Elastic properties

Since the material properties change with temperature and water uptake, a simplified FEMU procedure is applied to fine-tune the four elastic constants – E_{11}, E_{22}, G_{12}, and ν_{12} of the CFRP material system herein used. This simplification means that only GA was used as an optimisation procedure since there was no need to use LMA to solve this problem. The material properties of the same towpreg were tested [12] for an extended time and for higher temperatures. The experimental results with their standard deviations are presented in Table 2 and these values are considered as boundary limits for the elastic properties to fine-tune.

In order to improve the fine-tuning, the definitions of G_{23} and ν_{23} follow the considerations from Kuo et al. [43]. They are defined by:

$$\begin{aligned} G_{23} &= \frac{E_{22}}{2(1+\nu_{23})}, \\ \nu_{23} &= -\frac{E_{22}\left[E_{11}\left(\frac{1}{2}-\nu_{12}\right)+2G_{12}\nu_{12}^2\right]+\Lambda}{2E_{11}G_{12}}, \end{aligned} \tag{18}$$

where

$$\Lambda = \sqrt{E_{22}^2\left[E_{11}\left(\frac{1}{2}-\nu_{12}\right)+2G_{12}\nu_{12}^2\right]^2 - 4E_{11}G_{12}\left[E_{11}E_{22}\left(\frac{1}{2}-\nu_{12}\right)-G_{12}\left(E_{11}-2E_{22}\nu_{12}^2\right)\right]}. \tag{19}$$

Table 2
Non-aged (60 days at 23 °C, and relative humidity of 50%) and aged (60 days at 80 °C) elastic properties for the CFRP cylinders [12]. These properties are used for the cylinders without conditioning (ML).

Properties	Non-aged	Aged
E_{11}[GPa]	129.3 ± 3.6	119.7 ± 4.1
E_{22}[GPa]	9.11 ± 0.49	6.3 ± 0.8
G_{12}[GPa]	5.44 ± 0.023	3.89 ± 0.19
ν_{12}	0.322 ± 0.023	0.331 ± 0.011

These two parameters (G_{23} and ν_{23}) are derived solely by the four parameters listed above.

The experimental data available for the FEMU procedure is the instantaneous displacement. This point was chosen as it retains the effect of temperature and water uptake and disregards any viscous (creep) effects. The L_2-norm considers only one point and is defined as:

$$L_2 = \frac{1}{2}\left|1 - \frac{d^{\mathrm{N}}}{d^{\mathrm{E}}}\right|. \tag{20}$$

The upper limits of the elastic moduli are considered to simplify the problem and reduce the likelihood of having multiple solutions. Lower limits (average aged properties), and the limits on the Poisson's ratio ($\nu_{12} \in [0.30, 0.35]$), are kept fixed throughout the optimisation process, which is done in a sequential way: first the WRT case, and then the HW one. For cylinders under WRT conditioning, non-aged properties are considered upper limits. Then, the WRT converged properties are used as upper limits for the parameter identification of specimens under HW conditioning. This hypothesis is backed up by DMA experiments from [12], where one notices a reduction of the tangent elastic moduli for the same towpreg, winding angles, and under the same environmental conditions. Moreover, the work from Eggers et al. [13] reports that other mechanical responses were evaluated and this reduction is indeed observed. Hence, the elastic moduli are defined as follows: $E_{\alpha\beta}^{(-)} \geqslant E_{\alpha\beta}^{(\mathrm{WRT})} \geqslant E_{\alpha\beta}^{(\mathrm{HW})};\ \alpha, \beta = \{1, 2\}$. For ν_{12}, no hypothesis is made.

3.6. Creep constants identification

The experimental results for cases herein considered are presented in [13]. The creep behaviour for HW conditioning in all configurations has both primary and secondary stages well defined. Thus, the chosen creep model must consider both regions. A time-hardening creep strain-rate law can be defined as a function of the stress, time, and temperature (Norton-Bailey law), as follows [44]:

$$\dot{\varepsilon}^{cr} = f(\sigma, T, t), \tag{21}$$

where ε^{cr} is the equivalent creep strain, σ the stress, T and t are temperature and time, respectively, while $\dot{(\cdot)}$ denotes time derivative. Eq. (21) can be further simplified by neglecting any cross-effect between the parameters [44]. Thus:

$$\dot{\varepsilon}^{cr} = f_1(\sigma) f_2(t) f_3(T). \tag{22}$$

The creep model herein considered uses, essentially, a mixture of time-hardening and Norton models, for describing both primary and secondary creep stages. The creep strain rate is then defined as:

$$\dot{\varepsilon}^{\mathrm{cr}} = \dot{\varepsilon}^{\mathrm{N}} + \dot{\varepsilon}^{\mathrm{TH}}, \tag{23}$$

where:

$$\dot{\varepsilon}^{\mathrm{TH}} = C_1\sigma^{C_2}t^{C_3}\exp\left(\frac{-C_4}{T}\right), \tag{24}$$

$$\dot{\varepsilon}^{\mathrm{N}} = C_5\sigma^{C_6}\exp\left(\frac{-C_7}{T}\right), \tag{25}$$

in which $C_i, i = \{1 \dots 7\}$ are constants of the model and T is the temperature (Kelvin). It is important to notice that C_1 and C_5 correspond to constants that depend on the material and the creep mechanism; C_2 and C_6 define the creep stress indices; C_3 determines the time-hardening index; and C_4 and C_7 are related to Arrhenius law approach (temperature–dependence) for each model [45]; C_1 and C_5 may also vary for materials that react with moisture

[6]. It is valid to mention that these parameters are constant throughout the cylinder.

The creep strain is defined as:

$$\varepsilon^{cr} = \frac{C_1\sigma^{C_2}t^{C_3+1}}{C_3+1}\exp\left(\frac{-C_4}{T}\right) + C_5\sigma^{C_6}t\exp\left(\frac{-C_7}{T}\right), \tag{26}$$

which was obtained simply by integrating over time Eqs. (24) and (25).

A discussion on the values and ranges of variables can be found in the literature [44]. This is important since this optimisation procedure requires closed domains. Thus:

- C_1 and C_5: they must be positive to avoid violating strain energy principles. They also have order of 10^{-2} to 10^{-14} (relative to creep strain rate) [44], with time t in seconds.
- C_2 and $C_6 : \varepsilon^{cr}$ must have $1 \leqslant \mathcal{O}(\sigma) \leqslant 5$, which infers that the constants must not be necessarily bounded by these limits.
- C_3: due to the tendency of the strain $\times$ time curve, $-1 < C_3 \leqslant 0$.
- C_4 and C_7: although no information regarding the theoretical limits of these constants can be found in the literature, these constants are related to the creep activation energy. Considering average values for the activation energy (65 – 85 kJ/mol of CFRP) [46], gas constant, and temperature, the Arrhenius equation has an order of $-11 \leqslant \mathcal{O}(\exp(-C_4/T), \exp(-C_7/T)) \leqslant -7$.

Given the fact that C_1, C_4, C_5, and C_7 are influenced by similar effects, the model is further simplified to:

$$\varepsilon^{cr} = \frac{\widehat{C}_1\sigma^{C_2}t^{C_3+1}}{C_3+1} + \widehat{C}_5\sigma^{C_6}t, \tag{27}$$

hence, $\widehat{C}_1$ and $\widehat{C}_5$ vary with temperature, water uptake, and creep mechanism.

For the input parameters identification, these considerations are made:

- $\widehat{C}_1$ and $\widehat{C}_5$ vary with water uptake and temperature. For each configuration and conditioning, these constants must be evaluated. Moreover, their new domain is set as $-25 \leqslant \mathcal{O}\left(\widehat{C}_1, \widehat{C}_5\right) \leqslant -9$.
- C_2, C_3 and C_6 are solely dependent on the problem to be solved. Thus, they are independent of temperature and water uptake. They are obtained once for **HW** as it is the most sensitive response and then they are kept constant for other conditions.

Table 3
Parameters for GA procedures for the fine-tuning of the elastic properties.

# Elastic variables	n_{ind}	n_{gen}	Best Members	η	Mutation Chance	γ
4	40	60	8	1	1%	1

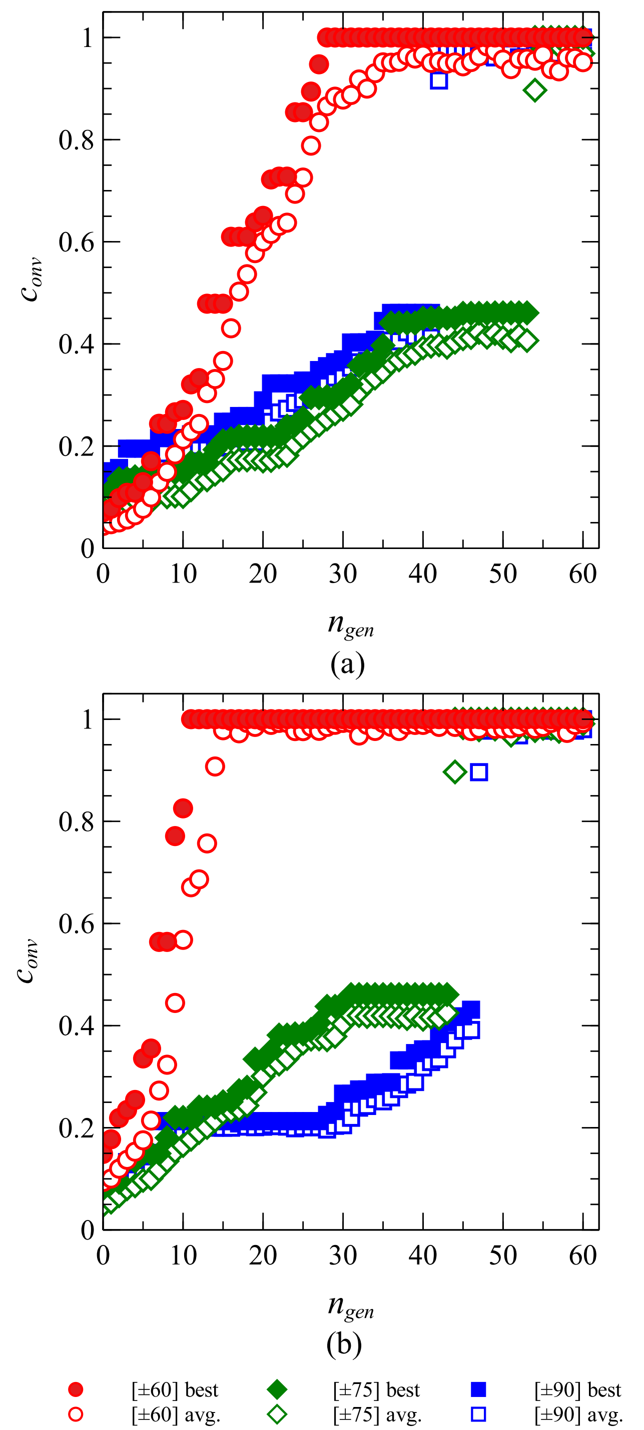

Fig. 5. Convergence of the GA for fine-tuning elastic properties. The best and average fitness are shown for (a) HW and (b) WRT conditions.

Table 4
Elastic properties for all cylinders wound at different fibre angles and under several environmental conditions obtained by FEMU.

Configuration		u_s [mm]	E_{11} [GPa]	E_{22} [GPa]	G_{12} [GPa]	ν_{12}	G_{23} [GPa]	ν_{23}	f_{it}
[±60]	WRT	4.10	127.87	9.09	5.43	0.348	2.63	0.728	1.06×10^{6}
	HW	4.17	124.57	8.95	5.42	0.345	2.59	0.727	4.33×10^{13}
[±75]	WRT	2.75	126.96	7.69	4.72	0.329	2.25	0.708	$> 10^{30}$
	HW	2.86	126.51	7.28	4.39	0.334	2.13	0.712	$> 10^{30}$
[±90]	WRT	2.30	122.40	7.42	4.89	0.311	2.18	0.701	$> 10^{30}$
	HW	2.32	121.76	7.03	3.99	0.303	2.14	0.642	$> 10^{30}$

Table 5
Parameters for GA and LMA optimisation procedures for creep parameters identification.

General						GA				LMA	
n_{ptos}	t_{ini} [s]	t_{fin} [s]	# n_{var}	n_{ind}	n_{gen}	Best Members	η	Mutation Chance	γ	$\Delta\rho_{ini}$	τ_{ini}
80	0	864000	5	50	35	10	1	1%	1	0.01	0.025

It is important to mention that the assessed points for the L_2-norm evaluation in the creep parameters identification follow an exponential space, which is constructed as:

$$t_i = \left\{ \frac{1}{n_{pts} - 1} \left[\sqrt{t_{fin}}(i-1) + \sqrt{t_{ini}}(n_{pts} - i) \right] \right\}^2, \tag{28}$$

where t_i, t_{fin}, and t_{ini} correspond to the time where the experimental and numerical data are assessed, final and initial points of both datasets, respectively. Essentially, considering that $t > 0$, a linear space is constructed over the square root of time and then passed onto the actual space. This results in approximately half of the assessed points being condensed to the third part of the evaluation time.

4. Results and discussion

4.1. Fine-tuning of elastic properties

The first step to identifying the creep constants is to fine-tune the elastic constants. This step is necessary since the well-known reduction of the properties given temperature and water uptake: the experimental data shows that the instantaneous displacement – without any viscous effect – is different given the conditioning. The optimisation procedure uses only the GA since the fitness values obtained were excellent, not requiring further steps with LMA. The parameters related to the optimisation procedure are listed in Table 3, in which the initial GA parameters have been taken from Almeida Jr et al. [47], which suit the current optimisation problem very well.

The obtained results are shown in Table 4, where u_s corresponds to the static displacement applied in each case and $G_{12} = G_{13}$ and $\nu_{12} = \nu_{13}$ for this geometry. The elastic moduli are slightly lower than those of non-conditioned specimens (Table 1 – non-aged properties). Also, the post-processed material parameters G_{23} and ν_{23} are also presented for the optimised sets. The high fitness indicates an excellent agreement between simulations and experiments. The convergence of the GA algorithm related to these results is depicted in Fig. 5, where the variable c_{onv} is written as:

$$c_{onv}^{(i)} = \frac{\log x_i}{\log x_{conv}}, \tag{29}$$

where i is the generation, x_i is the average fitness of the i-th generation, and x_{conv} is the best member at the last generation. Excluding the $\pm 60^\circ$, all other analyses reached the maximum possible fitness, perfectly matching the experimental data (u_s). And even for the worst-case, $\pm 60^\circ$ WRT, a value of $c_{onv} = 0.5$ means that the numerical value is 99.9% of the experimental one. Now, with elastic properties fine-tuned for each condition and winding angle, the elastic analysis is fully defined, and creep parameters can then be identified.

It is natural to assume that the objective function might have some global minima ($L_2 = 0$). To avoid those minima, a qualitative approach, relying on dynamic mechanical analyses (DMA) from Almeida Jr et al. [12], was carried out to understand the global behaviour of aged laminates. In general, it is assumed that aged properties are lower than non–aged ones [6–8]. For each condition, GA analyses were carried out and the sets of properties shown in Table 4 represent the best set of results considering i) the norm, ii) correlation with DMA data and iii) connection with aged properties from [12]. This series of qualitative analyses are crucial to increase the reliability of the data obtained and presented in Table 4, and this helps with the prediction of creep constants, which is presented next.

4.2. Creep parameters identification

For the sake of repeatability, all parameters used to find the optimum creep properties are listed in Table 5, whereas the upper and lower limits are presented in Table 6. In the GA step, the design variables are constrained to these values, whereas in the LMA step, they are used for mapping the parameters (Eqs. (16,17)).

The optimum creep constants obtained by the sequential FEMU procedure are presented in Table 7. The hypothesis of fixing C_2, C_3 and C_6 for all conditions explain why these constants vary with the winding angle only. This hypothesis seems adequate as the fitnesses of **WRT** and **ML** cases are higher than **HW**, with an exception for $[\pm 90]$-**WRT**.

Table 6
Upper and lower limits for GA, which are further utilised for mapping the LMA step.

Limits	# Design variables				
	$\widehat{C}_1$	C_2	C_3	$\widehat{C}_4$	C_5
Upper	10^{-9}	0.01	−0.99	10^{-9}	0.01
Lower	10^{-25}	5	0	10^{-25}	5

Table 7
Creep constants obtained by FEMU.

Stacking	Condition	$\widehat{C}_1$	C_2	C_3	$\widehat{C}_5$	C_6	f_{it}
$[\pm 60]$	HW	5.030×10^{-15}	3.802	−0.5489	1.884×10^{-12}	1.381	74.360
	WRT	1.727×10^{-15}			7.101×10^{-18}		135.047
	ML	9.286×10^{-16}			1.000×10^{-24}		201.803
$[\pm 75]$	HW	3.050×10^{-16}	3.836	−0.375	1.000×10^{-24}	1.536	93.877
	WRT	7.389×10^{-20}			2.223×10^{-14}		135.132
	ML	2.557×10^{-17}			3.635×10^{-14}		198.374
$[\pm 90]$	HW	3.401×10^{-18}	4.095	−0.118	7.562×10^{-24}	1.944	145.139
	WRT	4.947×10^{-19}			1.000×10^{-24}		59.422
	ML	3.774×10^{-19}			3.444×10^{-20}		101.629

The simulated creep curves, using the constants in Table 7, are compared to experimental data in Fig. 6. The correlation between numerical and experimental responses is excellent for all cases, which was impossible to achieve by running FEMU with a single algorithm (either GA or LMA). In all cases, both primary and secondary stages are properly identified, showing the efficiency of the approaches used in the FE model.

The creep curves shown in Fig. 6 are given for three winding angles: (a) $\pm 60^{\circ}$, (b) $\pm 75^{\circ}$ and (c) $\pm 90^{\circ}$. In general, the higher the fibre angle, the lower the displacement is over time. This is expected since off–axis layers (e.g., $\pm 60^{\circ}$ and $\pm 75^{\circ}$) are more dependent on the matrix, which has a viscoelastic response. Likewise, when fibres are oriented along the loading direction (i.e. radial compression), the deflection over time is lower since the response is controlled primarily by the fibres.

The environmental conditions affect all cylinders in a similar way. Regardless of the winding angle, specimens under ML have the lowest displacement. Adding water at room temperature (WRT) slightly increases the displacement over time. In contrast, hot water (HW) drastically increases the creep rate and hence has the highest deflection levels. This is expected since creep is time– and temperature–dependent, and, since the time is constant for all cylinders, the temperature has a strong influence on the

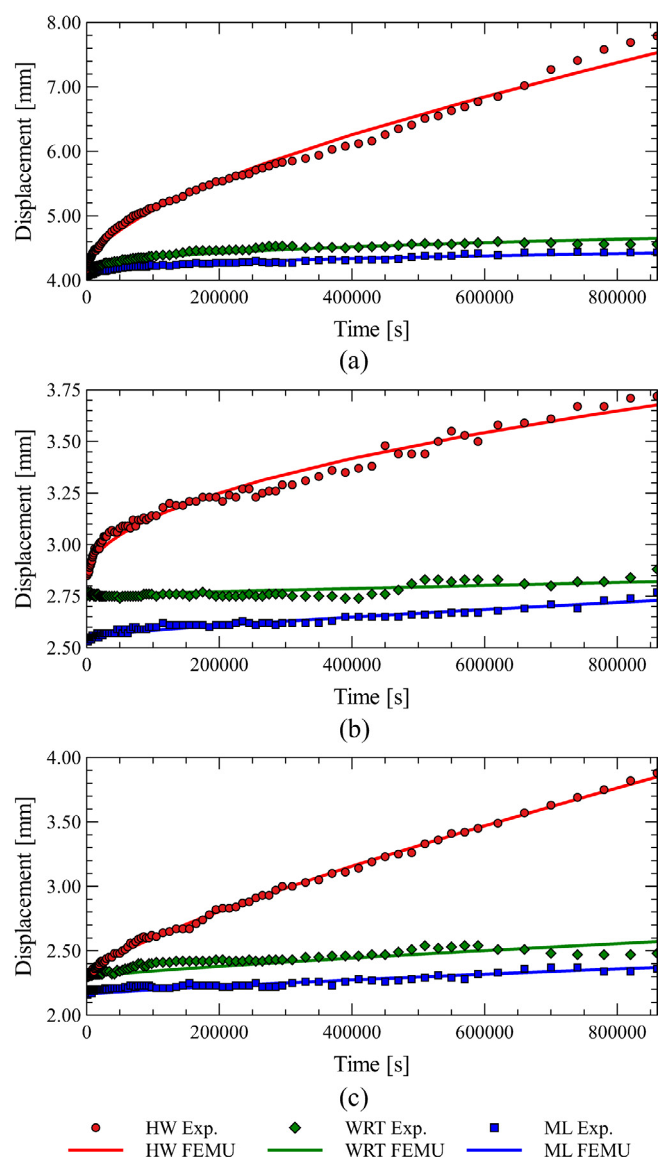

Fig. 6. Computational results from FEMU compared to experimental data for (a) [±60], (b) [±75], and (c) [±90] cylinders.

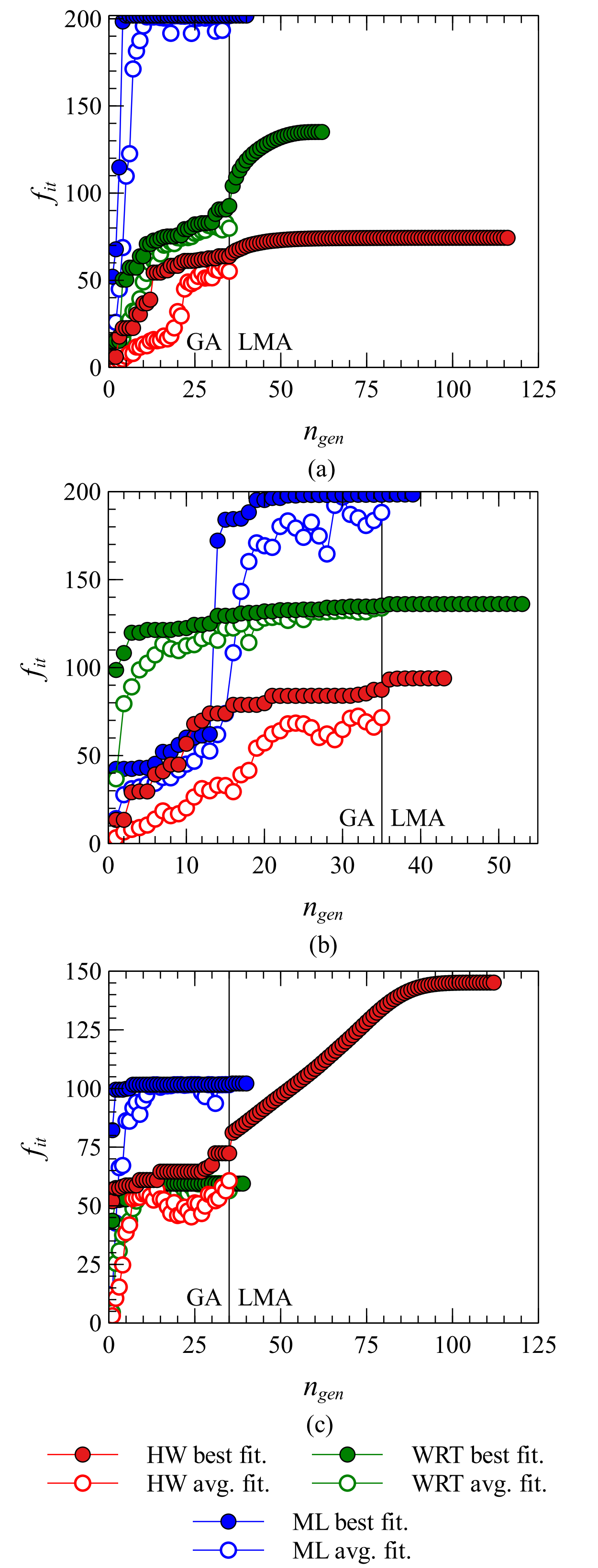

Fig. 7. Convergence of the GA and LMA optimisation procedures for (a) [±60] , (b) [±75], and (c) [±90] cylinders. The number of generations (n_{gen}) is also considered for the LMA steps.

creep response of the structures. Even though HW cylinders have a high creep rate throughout their secondary creep stage, they did not enter the tertiary creep stage.

The convergence characteristics of the GA–LMA for all cases are shown in Fig. 7. A vertical line separates the contribution of each step of FEMU. The results show that while GA goes through "jumps", LMA has a more "steady" behaviour while navigating around the objective function. This behaviour is noticed in the cases of [±60]-**HW**, [±60]-**WRT**, and [±90]-**HW**, with a focus on the latter.

Furthermore, it is important to explain why LMA has little influence on the **WRT** and **ML** conditions. In these two cases, only two design variables were optimised whereas the **HW** cylinders had five parameters. The reduced complexity meant that the GA algorithm could achieve, with the same number of generations, much better results and the global minimum is close to the LMA initial step.

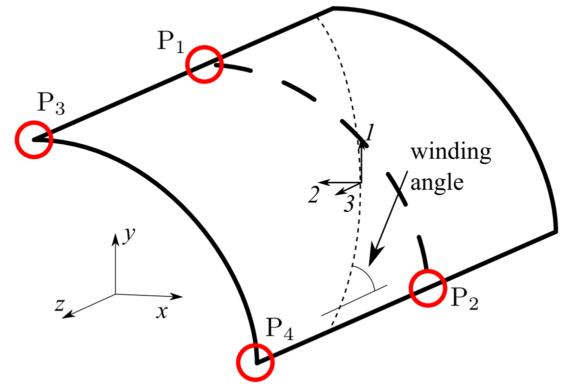

Fig. 8. The four points used to report stresses and strains. Points 1 and 3 are on the contact region, whereas points 2 and 4 are on the mid-section of the cylinder. The local coordinate system is aligned with the fibre direction.

4.3. Stress analysis

Although the main objective here is to introduce sequential optimisation to identify creep parameters, the simulations were also useful to compare the stresses and equivalent strain rates for the three winding angles and their different environmental conditions. Firstly, four points, shown in Fig. 8, were selected to present these results. Moreover, since shell elements were used in the FE model, the results are reported for both top and bottom surfaces.

The stresses at point 1 are given in Table 8 and those for point 2 are listed in Table 9 (see Fig. 8 for the location of both points). In each Table, values are given for σ_{11}, σ_{22}, and σ_{12} representing the stress along the fibre, matrix and in–plane shear directions, respectively. Each component of stress is given at four different times to capture the creep evolution. Important to mention that the shell elements used in this finite strain analysis allow for changes in thickness ($\varepsilon_{33} \neq 0$), and this variation is taken into account in the stress calculations.

Interestingly, without any viscous effects (0 s), the stress in the fibre direction is similar ($\approx$ 350 MPa) for all winding angles. In contrast, σ_{22} and σ_{12} vary. This behaviour is expected since creep is a phenomenon that is more pronounced on the polymer instead of the fibres, that is, transverse stresses are more affected by creep than longitudinal ones. Furthermore, at this stage, the stress field seems to be insensitive to environmental conditions. In all cases, the stress in the fibre direction σ_{11} decreases with time. This reduction is particularly important for the cylinder with 60° and HW, and it is more pronounced at point 1 rather than at point 2. In contrast, both σ_{22} and σ_{12} increase sharply with time. The HW cylinder with a fibre angle of 60° shows the largest variations in stresses.

During the creep loading, the cylindrical profile becomes an ellipsoidal and this effect is more pronounced for [±60] and HW samples. This change of shape rearranges the structural forces over the specimen and also increases the area of contact with the pla-

Table 8
Stress components at point 1 for both top and bottom surfaces of the cylinder. Values are in MPa and given at different times.

			TOP				BOTTOM			
Cond.		$\boldsymbol{\sigma}$	0 s	172,000 s	432,000 s	864,000 s	0 s	172,000 s	432,000 s	864,000 s
60°	HW	σ_{11}	−326.71	−212.43	−201.43	−194.06	350.73	185.02	168.06	155.59
		σ_{22}	−56.798	−76.719	−85.367	−93.820	8.5201	22.932	29.193	36.360
		σ_{12}	30.368	40.264	42.675	44.213	55.543	56.866	58.797	60.017
	WRT	σ_{11}	−328.31	−248.17	−232.83	−221.94	352.37	231.57	212.46	199.21
		σ_{22}	−56.744	−64.992	−67.488	−69.649	8.560	14.899	16.848	18.587
		σ_{12}	29.732	35.151	36.386	37.336	54.869	54.064	54.127	54.243
	ML	σ_{11}	−329.25	−269.86	−254.75	−243.19	353.44	259.31	239.52	224.97
		σ_{22}	−55.940	−61.564	−63.484	−65.208	7.8301	12.224	13.693	15.022
		σ_{12}	29.622	33.550	34.643	35.545	54.762	54.064	54.025	54.056
75°	HW	σ_{11}	−355.31	−256.57	−239.13	−228.18	359.29	232.56	213.56	201.98
		σ_{22}	−39.435	−46.167	−49.054	−51.756	−13.809	−6.686	−3.698	−0.7574
		σ_{12}	23.194	25.494	26.194	26.689	33.658	33.538	33.717	33.874
	WRT	σ_{11}	−351.68	−350.47	−348.86	−346.28	354.08	351.62	349.35	345.71
		σ_{22}	−39.494	−39.553	−39.768	−40.123	−13.467	−13.289	−13.144	−12.905
		σ_{12}	23.922	23.838	23.932	24.085	34.351	34.460	34.518	34.613
	ML	σ_{11}	−345.75	−322.75	−309.17	−295.81	342.80	310.45	292.94	276.42
		σ_{22}	−41.545	−42.664	−43.632	−44.835	−12.867	−11.411	−10.395	−9.1887
		σ_{12}	24.744	25.021	25.316	25.664	35.401	35.238	35.180	35.184
90°	HW	σ_{11}	−334.87	−266.55	−250.42	−244.02	334.78	266.65	250.49	244.02
		σ_{22}	−5.3425	−10.027	−13.979	−18.962	5.7682	10.468	14.441	19.451
		σ_{12}	−0.3564	−0.3064	−0.2799	−0.2599	0.3562	0.3071	0.2813	0.2619
	WRT	σ_{11}	−335.01	−310.64	−292.50	−276.53	334.92	310.64	292.56	276.62
		σ_{22}	−5.9802	−7.0207	−8.0585	−9.3667	6.4314	7.4714	8.5098	9.8211
		σ_{12}	−0.4089	−0.3962	−0.3840	−0.3705	0.4088	0.3965	0.3845	0.3712
	ML	σ_{11}	−334.55	−314.21	−297.78	−282.20	334.46	314.21	297.83	282.28
		σ_{22}	−7.2396	−8.2008	−9.1965	−10.462	7.7487	8.7073	9.7013	10.966
		σ_{12}	−0.4105	−0.4000	−0.3898	−0.3776	0.4103	0.4002	0.3902	0.3783

Table 9
Stress components at point 2 for both top and bottom surfaces of the cylinder. Values are in MPa and given at different times.

Cond.		σ	TOP 0 s	TOP 172,000 s	TOP 432,000 s	TOP 864,000 s	BOTTOM 0 s	BOTTOM 172,000 s	BOTTOM 432,000 s	BOTTOM 864,000 s
60°	HW	σ_{11}	179.69	143.46	131.68	122.59	−179.44	−144.69	−133.52	−125.07
		σ_{22}	18.829	24.721	28.944	34.165	−21.153	−26.936	−31.129	−36.278
		σ_{12}	−21.366	−24.807	−27.297	−30.065	−21.121	−24.956	−27.605	−30.508
	WRT	σ_{11}	180.66	165.75	160.10	155.09	−180.35	−166.12	−160.64	−155.75
		σ_{22}	18.836	20.358	20.980	21.586	−21.172	−22.628	−23.225	−23.809
		σ_{12}	−21.038	−21.842	−22.162	−22.477	−20.781	−21.728	−22.106	−22.476
	ML	σ_{11}	181.17	172.19	168.26	164.50	−180.83	−172.33	−168.55	−164.91
		σ_{22}	18.427	19.357	19.758	20.159	−20.770	−21.659	−22.044	−22.429
		σ_{12}	−20.974	−21.468	−21.672	−21.876	−20.708	−21.287	−21.528	−21.769
75°	HW	σ_{11}	186.13	169.29	161.34	154.92	−188.30	−171.24	−163.22	−156.75
		σ_{22}	7.4495	8.8926	9.7640	10.704	−10.760	−12.074	−12.859	−13.708
		σ_{12}	−15.125	−16.010	−16.494	−17.001	−15.215	−16.157	−16.676	−17.218
	WRT	σ_{11}	183.45	183.28	182.79	181.99	−185.76	−185.62	−185.14	−184.37
		σ_{22}	7.5491	7.6006	7.6767	7.8027	−10.836	−10.895	−10.969	−11.092
		σ_{12}	−15.495	−15.547	−15.598	−15.681	−15.595	−15.646	−15.699	−15.785
	ML	σ_{11}	178.56	176.69	174.87	172.48	−181.15	−179.24	−177.40	−174.80
		σ_{22}	8.2541	8.5001	8.7469	9.0996	−11.607	−11.842	−12.072	−12.402
		σ_{12}	−16.049	−16.205	−16.342	−16.536	−16.157	−16.316	−16.460	16.661
90°	HW	σ_{11}	197.86	190.14	185.04	182.62	−203.51	−193.13	−186.95	−184.08
		σ_{22}	3.5615	4.6671	5.8848	7.6164	−3.5272	−4.6418	−5.8566	−7.5751
		σ_{12}	−0.0043	−0.0046	−0.0051	−0.0059	−0.0086	−0.0086	−0.0087	−0.0092
	WRT	σ_{11}	197.88	196.58	194.99	192.77	−203.46	−201.56	−199.36	−196.43
		σ_{22}	3.8170	3.9995	4.2171	4.5344	−3.7866	−3.9709	−4.1914	−4.5117
		σ_{12}	−0.0049	−0.0047	−0.0049	−0.0050	−0.0090	−0.0090	−0.0089	−0.0089
	ML	σ_{11}	197.29	196.26	194.98	193.15	−202.85	−201.34	−199.56	−197.10
		σ_{22}	4.5638	4.7296	4.9283	5.2195	−4.5627	−4.7307	−4.9329	−5.2285
		σ_{12}	−0.0052	−0.0051	−0.0051	−0.0053	−0.0094	−0.0093	0.0093	−0.0092

tens. All these changes have, consequently, an influence on the stress distribution in the sample. It was observed a stress transfer from the fibre to the matrix, and a similar observation was also found by Rafiee and Ghorbanhosseini [48], where the stresses in the fibre direction were reduced during creep loading for glass fibre–reinforced composite polyester cylinders in radial compression. Hence, forces and stresses on the structure change due to eccentricity effects, whose response is more pronounced for the [±60] samples, given that this is the off–axis fibre angle further away from the fibre angle in the loading direction when compared with other samples (e.g., 90°).

The large stress variations due to creep can have significant effects on the safety coefficients and in–service margins employed in the design. As mentioned, the variations are detrimental since there is a stress reduction in the fibre direction (σ_{11}) but an increase in the transverse directions (σ_{22} and σ_{12}) [12]. Consider, for example, an HW cylinder wound at 60°. With the stress field at P_2-bottom (and using non-aged properties from [12]), the instantaneous (0 s) and 10–day (864 s) failure index (Tsai-Wu failure criterion [49]) is 0.387 and 0.892, respectively. This represents a considerable increase of ~230%.

These stress variations are attributed to three factors: i) creep deformation is changing the initial cross-section from a circle to an ellipse [50], reducing the effective stiffness of the cylinder, ii) the load redistribution due to the contact with the compressive platens, and iii) non-linear effects. As observed by Lisbôa et al. [2,32], during the initial loading stage, the force × displacement curve is mostly linear–elastic. At an intermediate stage, this behaviour changes slightly, and the cylinder becomes more compliant. At the final stage, the specimen becomes slightly stiffer again, nonetheless, this effect is to some extent shadowed by major cracking on the cylinder (i.e., damage initiation). In creep experiments, the deflection increases up to the secondary creep stage, in which some softening is observable, mostly for the HW condition. Furthermore, as the cross-section becomes elliptical (Fig. 9), the contact area between the cylinder and platen increases and, as the force is a fixed parameter, the contact stresses are reduced. This can explain the larger stress variations at point 1 (contact area) compared to point 2. Moreover, it is also worth mentioning

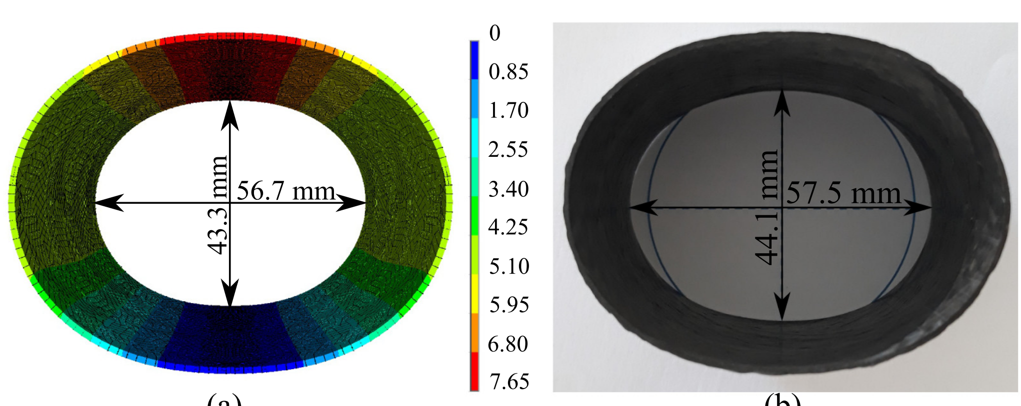

Fig. 9. Comparison between (a) numerical and (b) experimental deformed shapes for the cylinder 60° (HW). The colour bar represents the predicted vertical displacement. The photograph of the test was taken after unloading.

the excellent prediction capability of the model in which the cross-section measurements are in excellent agreement. The difference in the major and minor axes measurements is because the experimental values were taken after the sample was unloaded, in which stress relaxation is unavoidable.

A comparison between the numerical and experimental deformation modes is shown in Fig. 9 for the 60° (HW) cylinder. The deformed shape and eccentricity in the simulations are in good agreement with the experiments. The major and minor axes are 1–2% larger in the experiment because the photograph was taken after unloading (whereas there is no unloading in the simulation).

The equivalent strain rate is plotted in Fig. 10 as a function of time. The strain rate is given for the four points identified earlier in Fig. 8. All cases exhibit a similar decreasing response except for Fig. 10(e), where the strain rate is almost constant. This means that the time-hardening effects are almost absent; indeed, the measured displacement for [±75]-(WRT) is practically constant over time, see Fig. 6(b). Consequently, $\widehat{C}_1$ is the smallest in all cases, see Table 7. For all other cases, the strain rate starts at a high value and decreases with time. This

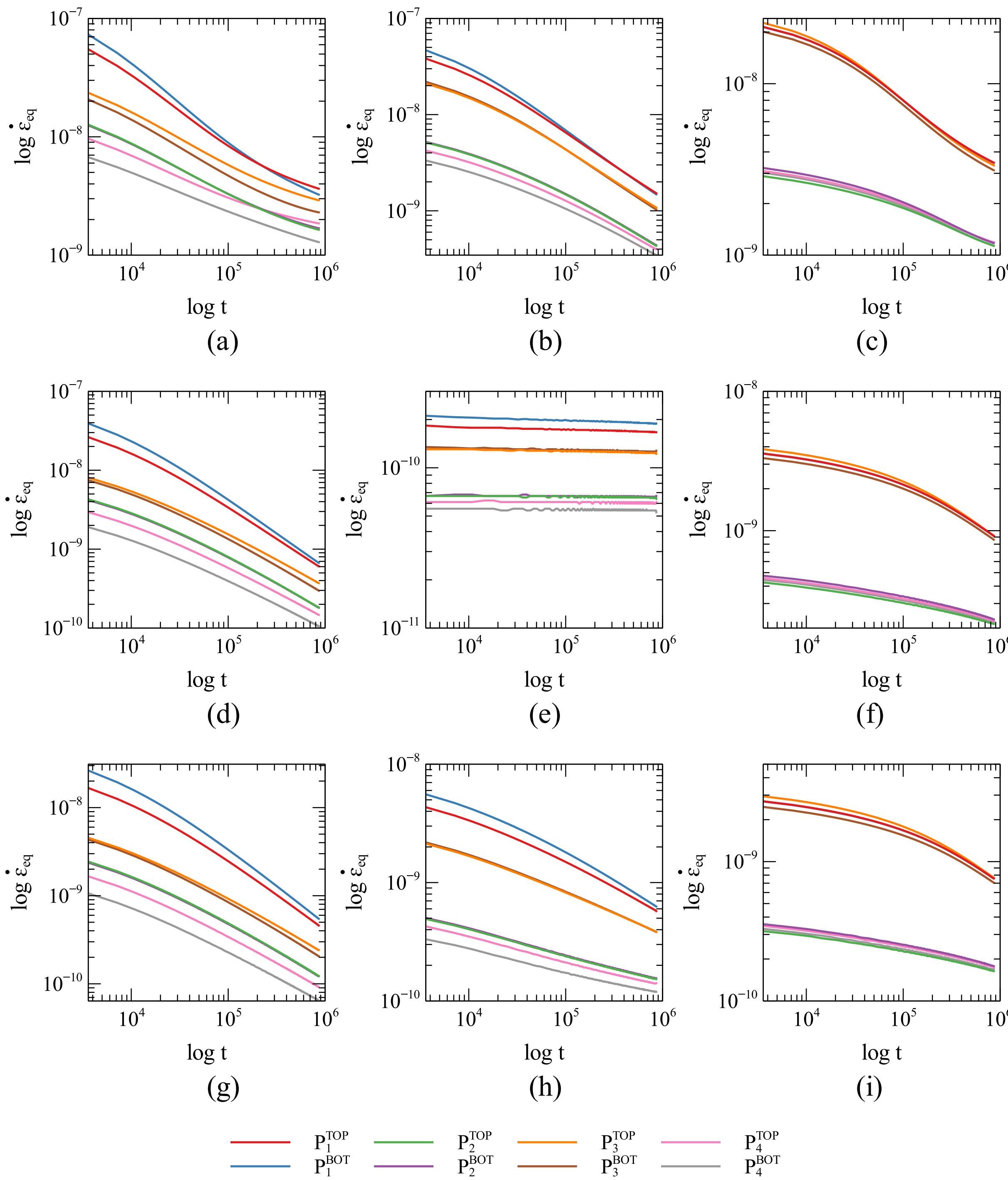

Fig. 10. Log–log plots of the equivalent strain rate as a function of time. Results are given at the four points shown in Fig. 8, and for (a) 60° (HW), (b) 75° (HW), (c) 90° (HW), (d) 60° (WRT), (e) 75° (WRT), (f) 90° (WRT), (g) 60° (ML), (h) 75° (ML), and (i) 9.0° (ML).

decrease tends to slow down after the $3^{rd}/4^{th}$ day, which corroborates with the displacement versus time curves (see Fig. 6) and and indicates the beginning of the second stage of creep. The results also indicate that the contact areas (points 1 and 3) have higher strain rates than the midsection (points 2 and 4). This is attributed to the elevated stress in these areas (see Tables 8,9).

As can be seen, the optimisation problem here is well solved in a computationally–efficient way and with a high degree of accuracy, which demonstrates the capability of the proposed sequential FEMU framework. Other approaches to solving the same problem might also be suitable, such as the use of deep neural networks to approximate the functions herein utilised for training the FE models [51] along with uncertainties from experimental observations (e.g., manufacturing and testing uncertainties.

5. Conclusions

An original finite element model updating framework has been here developed as a new method to identify the creep parameters of filament wound cylinders under different harsh environmental conditions. An original FE model is developed, in which the winding pattern is taken into consideration. All cylinders were subjected to radial compressive creep loading for 10 days. The framework is based on a sequential optimisation that starts with a heuristic genetic algorithm and finishes with the gradient–based Levenberg–Marquardt algorithm, aiming at reducing and/or avoiding the likelihood of finding local minima. The results were in excellent agreement with experimental observations, which indicates that the computational model and its hypotheses were well formulated.

After identifying the parameters of the creep model, the stresses and equivalent strain rate were exported from the FE model and interesting characteristics were observed: i) the softening of the cylinders due to the circular-to-elliptic transformation of the cross-section, ii) a more pronounced reduction in the transverse direction than in the longitudinal one (typical of creep consequences for continuous fibre–reinforced laminates with off–axis plies), iii) the natural reduction of failure index as a consequence of point ii), even with the same applied load. These results strengthen the importance of creep behaviour analysis in composite structures exposed to harsh environments. This framework can augment the experimental data, reduce experimental costs (since creep tests are expensive and time–consuming), and elucidate creep effects on FW composite cylinders exposed to harsh environments with an efficient computational tool. Future work will consider the implementation of higher–order finite element formulations to increase the accuracy of transverse and out–of–plane stress fields for structures under creep loading.

Declaration of Competing Interest

The authors declare that they have no known competing financial interests or personal relationships that could have appeared to influence the work reported in this paper.

Acknowledgements

HA is supported by the Royal Academy of Engineering under the Research Fellowship scheme [Grant No. RF/201920/19/150]. We also thank CAPES/DAAD (Probral project 88881.198774/2018-01 and 57447163) for their financial support.

References

[1] Almeida Jr JHS, Tonatto MLP, Ribeiro ML, Tita V, Amico SC. Buckling and post-buckling of filament wound composite tubes under axial compression: Linear, nonlinear, damage and experimental analyses. Compos Part B: Eng 2018;149:227–39.
[2] Lisbôa TV, Almeida Jr JHS, Dalibor IH, Spickenheuer A, Marczak RJ, Amico SC. The role of winding pattern on filament wound composite cylinders under radial compression. Polym Compos 2020;41(6):2446–54.
[3] Almeida Jr JHS, Faria H, Marques AT, Amico SC. Load sharing ability of the liner in type III composite pressure vessels under internal pressure. J Reinf Plast Compos 2014;33(24):2274–86.
[4] Minsch N, Müller M, Gereke T, Nocke A, Cherif C. 3d truss structures with coreless 3d filament winding technology. J Compos Mater 2019;53(15):2077–89.
[5] Yang Z, Wang H, Ma X, Shang F, Ma Y, Shao Z, et al. Flexural creep tests and long-term mechanical behavior of fiber-reinforced polymeric composite tubes. Compos Struct 2018;193:154–64.
[6] Brinson LC, Gates TS. Effects of physical aging on long term creep of polymers and polymer matrix composites. Int J Solids Struct 1995;32(6):827–46.
[7] Sullivan JL. Creep and physical aging of composites. Compos Sci Technol 1990;39(3):207–32.
[8] Sullivan JL, Blais EJ, Houston D. Physical aging in the creep behavior of thermosetting and thermoplastic composites. Compos Sci Technol 1993;47(4):389–403.
[9] Guedes RM, Morais JJL, Marques AT, Cardon AH. Prediction of long-term behaviour of composite materials. Comput Struct 2000;76(1):183–94.
[10] Nguyen S-N, Lee J, Han J-W, Cho M. A coupled hygrothermo-mechanical viscoelastic analysis of multilayered composite plates for long-term creep behaviors. Compos Struct 2020;242:112030.
[11] Botelho EC, Pardini LC, Rezende MC. Damping behavior of hygrothermally conditioned carbon fiber/epoxy laminates. J Appl Polym Sci 2007;106(5):3143–8.
[12] Almeida Jr JHS, Souza SDB, Botelho EC, Amico SC. Carbon fiber-reinforced epoxy filament-wound composite laminates exposed to hygrothermal conditioning. J Mater Sci 2016;51:4697–708.
[13] Eggers F, Almeida Jr JHS, Lisbôa TV, Amico SC. Creep and residual properties of filament-wound composite rings under radial compression in harsh environments. Polymers 2021;13(1).
[14] Keller MW, Jellison BD, Ellison T. Moisture effects on the thermal and creep performance of carbon fiber/epoxy composites for structural pipeline repair. Compos Part B: Eng 2013;45(1):1173–80.
[15] Scattina A, Roncato D, Belingardi G, Martino G. Investigation of creep phenomenon on composite material for bolt connections. Compos Struct 2015;134:378–83.
[16] Almeida Jr JHS, Ornaghi Jr HL, Lorandi N, Marinucci G, Amico SC. On creep, recovery, and stress relaxation of carbon fiber-reinforced epoxy filament wound composites. Polym Eng Sci 2018;58(10):1837–42.
[17] Rafiee R, Habibagahi MR. Evaluating mechanical performance of gfrp pipes subjected to transverse loading. Thin-Walled Struct 2018;131:347–59.
[18] Erkmen RE, Bradford MA. Time-dependent creep and shrinkage analysis of composite beams curved in-plan. Comput Struct 2011;89(1):67–77.
[19] Rafiee R, Ghorbanhosseini A. Analyzing the long-term creep behavior of composite pipes: Developing an alternative scenario of short-term multi-stage loading test. Compos Struct 2020;254:112868.
[20] Reddy JN. A general non-linear third-order theory of plates with moderate thickness. Int J Non-Linear Mech 1990;25(6):677–86.
[21] Carrera E. Theories and finite elements for multilayered plates and shells:a unified compact formulation with numerical assessment and benchmarking. Arch Comput Methods Eng 2003;10(3):215–96.
[22] Pagani A, Carrera E. Large-deflection and post-buckling analyses of laminated composite beams by carrera unified formulation. Compos Struct 2017;170:40–52.
[23] Ferreira GFO, Almeida Jr JHS, Ribeiro ML, Ferreira AJM, Tita V. Development of a finite element via unified formulation: Implementation as a user element subroutine to predict stress profiles in composite plates. Thin-Walled Struct 2020;157:107107.
[24] Demasi L. $\infty 6$ mixed plate theories based on the generalized unified formulation. part i: Governing equations. Compos Struct 2009;87(1):1–11.
[25] Carrera E. Theories and finite elements for multilayered, anisotropic, composite plates and shells. Arch Comput Methods Eng 2002;9(2):87–140.
[26] Ferreira GFO, Almeida Jr JHS, Ribeiro ML, Ferreira AJM, Tita V. A finite element unified formulation for composite laminates in bending considering progressive damage. Thin-Walled Struct 2022;172:108864.
[27] Caliri MF, Ferreira AJM, Tita V. Through-the-thickness stress profiles in laminated composite and sandwich structure plates via unified formulation. Compos Part B: Eng 2016;107:29–42.
[28] Duan X, Yuan H, Tang W, He J, Guan X. A phenomenological primary–secondary–tertiary creep model for polymer-bonded composite materials. Polymers 2021;13(14).
[29] Tanks J, Rader K, Sharp S, Sakai T. Accelerated creep and creep-rupture testing of transverse unidirectional carbon/epoxy lamina based on the stepped isostress method. Compos Struct 2017;159:455–62.

[30] Rafiee R, Mazhari B. Evaluating long-term performance of glass fiber reinforced plastic pipes subjected to internal pressure. Constr Build Mater 2016;122:694–701.
[31] Corveleyn S, Lachaud F, Berthet F, Rossignol C. Long-term creep behavior of a short carbon fiber-reinforced peek at high temperature: Experimental and modeling approach. Compos Struct 2022;290:115485.
[32] Lisbôa TV, Almeida Jr JHS, Spickenheuer A, Stommel M, Amico SC, Marczak RJ. FEM updating for damage modeling of composite cylinders under radial compression considering the winding pattern. Thin-Walled Struct 2022;173:108954.
[33] Jin S-S, Jung H-J. Sequential surrogate modeling for efficient finite element model updating. Comput Struct 2016;168:30–45.
[34] Bresolin FL, Vassoler JM. A numerical study of the constitutive characterization of thermoplastic materials submitted to finite strain. Int J Solids Struct 2020;206:456–71.
[35] Elouneg A, Sutula D, Chambert J, Lejeune A, Bordas SPA, Jacquet E. An open-source fenics-based framework for hyperelastic parameter estimation from noisy full-field data: Application to heterogeneous soft tissues. Comput Struct 2021;255:106620.
[36] Giagopoulos D, Arailopoulos A. Computational framework for model updating of large scale linear and nonlinear finite element models using state of the art evolution strategy. Comput Struct 2017;192:210–32.
[37] Almeida Jr JHS, Ornaghi Jr HL, Lorandi N, Bregolin BG, Amico SC. Creep and interfacial behavior of carbon fiber reinforced epoxy filament wound laminates. Polym Compos 2018;39(S4):E2199–206.
[38] Eggers F, Almeida Jr JHS, Azevedo CB, Amico SC. Mechanical response of filament wound composite rings under tension and compression. Polym Test 2019;78:33. 105951.
[39] Almeida Jr JHS, Ribeiro ML, Tita V, Amico SC. Damage modeling for carbon fiber/epoxy filament wound composite tubes under radial compression. Compos Struct 2017;160:204–10.
[40] Deb K, Agrawal RB. Simulated binary crossover for continuous search space. Complex Syst 1995;9(2):115–48.
[41] Zhao X, Gao X-S, Hu Z-C. Evolutionary programming based on non-uniform mutation. Appl Math Comput 2007;192(1):1–11.
[42] Kanzow C, Yamashita N, Fukushima M. Levenberg–marquardt methods with strong local convergence properties for solving nonlinear equations with convex constraints. J Comput Appl Math 2004;172(2):375–97.
[43] Kuo Y-M, Lin H-J, Wang C-N, Liao C-I. Estimating the elastic modulus through the thickness direction of a uni-direction lamina which possesses transverse isotropy property. J Reinf Plast Compos 2007;26(16):1671–9.
[44] Hu J, Chen W, Li Y, Qu Y, Zhao B, Yang D. Temperature stress-time methodology for flat-patterning etfe cushions in use for large span building structures. Eng Struct 2020;204:109607.
[45] Alwis KGNC, Burgoyne CJ. Time-temperature superposition to determine the stress-rupture of aramid fibres. Appl Compos Mater 2006;13(4):249–64.
[46] Cruz-Cruz I, Ramírez-Herrera CA, Martínez-Romero O, Castillo-Márquez SA, Jiménez-Cedeño IH, Olvera-Trejo D, Elías-Zúñiga A. Influence of epoxy resin curing kinetics on the mechanical properties of carbon fiber composites. Polymers 2022;10(6):1100.
[47] Almeida Jr JHS, Bittrich L, Nomura T, Spickenheuer A. Cross-section optimization of topologically-optimized variable-axial anisotropic composite structures. Compos Struct 2019;225:111150.
[48] Rafiee Roham, Ghorbanhosseini Amin. Developing a micro-macromechanical approach for evaluating long-term creep in composite cylinders. Thin-Walled Struct 2020;151:106714.
[49] Tsai SW, Wu EM. A general theory of strength for anisotropic materials. J Compos Mater 1971;5(1):58–80.
[50] Tse PC, Lai TC, So CK, Cheng CM. Large deflection of elastic composite circular springs under uniaxial compression. Int J Non-Linear Mech 1994;29(5):781–98.
[51] Samaniego E, Anitescu C, Goswami S, Nguyen-Thanh VM, Guo H, Hamdia K, et al. An energy approach to the solution of partial differential equations in computational mechanics via machine learning: Concepts, implementation and applications. Comput Methods Appl Mech Eng 2020;362:112790.